

**ANALYSIS OF THE FORCINGS OF THE
PACIFIC DECADAL OSCILLATION IN CCSM4**

by

Christina A. Finan

A thesis submitted to the Faculty of the University of Delaware in partial fulfillment of the requirements for the degree of Master of Science in Geography

Summer 2014

© 2014 Christina A. Finan
All Rights Reserved

UMI Number: 1567804

All rights reserved

INFORMATION TO ALL USERS

The quality of this reproduction is dependent upon the quality of the copy submitted.

In the unlikely event that the author did not send a complete manuscript and there are missing pages, these will be noted. Also, if material had to be removed, a note will indicate the deletion.



UMI 1567804

Published by ProQuest LLC (2014). Copyright in the Dissertation held by the Author.

Microform Edition © ProQuest LLC.

All rights reserved. This work is protected against unauthorized copying under Title 17, United States Code



ProQuest LLC.
789 East Eisenhower Parkway
P.O. Box 1346
Ann Arbor, MI 48106 - 1346

**ANALYSIS OF THE FORCINGS OF THE
PACIFIC DECADAL OSCILLATION IN CCSM4**

by

Christina A. Finan

Approved: _____
Brian Hanson, Ph.D.
Professor in charge of thesis on behalf of the Advisory Committee

Approved: _____
Tracy L. DeLiberty, Ph.D.
Chair of the Department of Geography

Approved: _____
Nancy M. Targett, Ph.D.
Dean of the College of Earth, Ocean, and Environment

Approved: _____
James G. Richards, Ph.D.
Vice Provost for Graduate and Professional Education

ACKNOWLEDGMENTS

I would like to thank the University of Delaware Geography Department for the opportunity to perform the research presented here, which would not have been possible without the education, resources and funding provided. To my advisor, Dr. Brian Hanson, I give many thanks for the encouragement, support and faith in me, even when I was not wholly convinced of my abilities. I leave this program equipped with the skills and knowledge for a successful career, as well as confidence, resultant from Brian's mentoring and positive, sometimes humorous, outlook. I also would like to thank the other members of my committee, Dr. Dan Leathers and Dr. Fabrice Veron, for their constructive insight and guidance. This work also is a product of the compassionate environment fostered by all the graduate students within the Department of Geography. I am grateful for all their support, direct and indirect, through education, coursework, and overall experience in the process of completing this thesis. Finally, to my family and friends, I have overwhelming gratitude for their unwavering love and belief in my determination and for helping me to pursue my aspirations.

TABLE OF CONTENTS

LIST OF FIGURES	vi
ABSTRACT	vii
Chapter	
1 INTRODUCTION AND LITERATURE REVIEW	1
1.1 Introduction	1
1.2 Literature Review	1
1.2.1 Pacific Decadal Oscillation and Its History.....	1
1.2.2 PDO and Proposed Cycle	3
1.2.3 PDO in Models	6
1.2.4 Model History.....	8
2 METHODS.....	10
2.1 Model Description	10
2.2 Model Components	10
2.2.1 Atmospheric Model	10
2.2.2 Land Model	11
2.2.3 Ocean Model	12
2.2.4 Sea Ice Model	13
2.2.5 Coupler	13
2.3 Run Specifications.....	13
3 RESULTS.....	15
3.1 EOF Analysis.....	15
3.1.1 Spatial Representation.....	16
3.1.2 Temporal Patterns.....	18
3.2 Time Series Analysis.....	18
3.3 Filtering	19

3.3.1	Filtered Results	20
3.4	Lag Correlations	21
3.4.1	North Pacific SST Lag Correlations	22
3.4.2	Lag Correlations between Other Components	22
4	DISCUSSION AND CONCLUSIONS	32
4.1	EOF Spatial and Temporal Patterns	32
4.1.1	Representation and analysis	32
4.2	Spectral Densities	32
4.3	Lag Correlations	33
4.3.1	Connections with the North Pacific SST field	33
4.3.2	Connections between other components	35
4.4	Conclusions	37
	REFERENCES	39
Appendix		
A	EQUATIONS FOR MODEL COMPONENTS	43

LIST OF FIGURES

Figure 1.1	The Pacific Decadal Oscillation Phases.....	9
Figure 3.1	First EOFs of Variable Fields.....	24
Figure 3.2	Modeled EOF vs. Observational EOF.....	25
Figure 3.3	Yearly Average Anomalies	26
Figure 3.4	Spectral Densities of Variable Fields	27
Figure 3.5	Filtered Yearly Average Anomalies.....	28
Figure 3.6	Filtered Spectral Densities of Variable Fields.....	29
Figure 3.7	Lag Correlations with North Pacific SSTs	30
Figure 3.8	Lag Correlations between Other Variables	31

ABSTRACT

The Pacific Decadal Oscillation (PDO), a variation of sea surface temperatures in the North Pacific Ocean, is analyzed using modeled output from the Community Climate System Model (CCSM) 4.0. The proposed forcings which cause this variation are fluctuations in the El Nino Southern Oscillation cycle, the Hadley cell circulation, the sea level pressure field and the western boundary current in the North Pacific, comprising a cycle outlined by DiLorenzo et al, 2010. This study uses modeled output as opposed to observational data due to temporal and spatial coverage available to replicate the components of the cycle. The spatial patterns are represented with the first empirical functions of each field and the temporal patterns are represented by the time series of annual averages centered on the winter season. The correlations between the other components and the PDO index indicate that they vary on the same time scale. Lag correlation is used to understand how the proposed components change in relation to each other temporally to map out the possible cycle in the model output. Results showed that the eastern Pacific fields responded faster than the western Pacific field, with a lag of 1 year compared to a lag of 5 years. Many of the lags found between components were consistent with past studies, while other varied slightly.

Chapter 1

INTRODUCTION AND LITERATURE REVIEW

1.1 Introduction

Oscillations and climatic variations control and modulate much of the Earth's atmospheric and oceanic conditions. Many of these vary on decadal to multidecadal timescales and much is unknown about what forces these longer term patterns to change phase. The Pacific Decadal Oscillation, a sea surface temperature variation in the North Pacific, is an example of an oceanic pattern that can have implications for precipitation and temperature conditions across the globe. To better understand what forces this oscillation, modeled output is used to study the mechanisms behind the phase changes.

1.2 Literature Review

1.2.1 Pacific Decadal Oscillation and Its History

The Pacific Decadal oscillation (PDO) was defined by Steven Hare and Nathan Mantua, during their research on the productivity of salmon fisheries in the Pacific Ocean (Hare & Mantua 1997). In their studies, the PDO was characterized by two main areas of interest, one in the central North Pacific and one along the coast of western North America, which have opposing sea surface temperature anomalies. The area along the coast is usually characterized as a horseshoe-shaped pattern, while the central Pacific is a large pool that extends to Japan and eastern Asia, as displayed in

Figure 1.1 (Mantua & Hare 1997). It has been more explicitly defined as the first empirical orthogonal function (EOF) of sea surface temperatures in the North Pacific. The SST anomalies have a periodicity, switching polarity every fifteen to twenty years, which is why the oscillation is referred to as interdecadal.

The validity of the PDO as its own independent variation and its classification as an oscillation has been questioned in many studies since the definition of the phenomenon. The oscillatory features of this variation have not been confirmed, nor has its genesis and all the forcings associated with its cycle. There has been speculation on whether the oscillation is a longer term variation of the El Niño Southern Oscillation (ENSO) cycle that propagates to the subtropics.

The climatological community has labeled the PDO as an oscillation, despite lack of evidence that a PDO phase change eventually causes the opposite phase to manifest. An oscillation typically would cause a negative feedback, which would induce the fluctuation from one phase to the opposing phase. One theory is that the PDO is actually just red noise instead of a true oscillation. Red noise results from natural fluctuations in environmental systems that are a product of memory from previous states of the system and random noise (Roe 2009). This would indicate that the changes in the PDO are not solely causing the oscillation to occur, but rather random noise also would play a key role in the variation of the north Pacific SSTs. The spectral estimate of the PDO at a 95% confidence interval lies within the bounds of a best fit for red noise with one-year memory (Roe 2009). Most of its variance does not greatly differ from red noise (Deser et al 2011). However, there still exists evidence that the PDO is its own distinct variation.

Tree ring data give a longer term record of the changes and reversals in the PDO due to its effect on precipitation in the western United States. In the tree ring data, a 23 year oscillation is seen consistently from 1661 to 1991, the entire length of the record (Bondi 2001). Lower frequency signals are only seen in the twentieth century. The PDO modulates ENSO, causing a more dramatic climate response when the two oscillations are in phase, which is seen more frequently in the twentieth century (Bondi 2001). The PDO signal exists in the tree records separately from the ENSO signal, especially before the later 1800's (Bondi 2001).

1.2.2 PDO and Proposed Cycle

Understanding the cycle of the PDO and its physical forcings would aid in distinguishing it as a discrete climatic oscillation. The genesis of the PDO and the cause for phase changes is unknown. There have been many studies on possible reasons for the oscillation, outlining other changes in the surrounding areas that have been observed to correspond or precede the phase changes (Kwon et al. 2012, Yeo et al. 2012, Park et al. 2013). In a study by DiLorenzo, a specific cycle in the Pacific is outlined which includes both oceanic and atmospheric forcings. The cycle has four main components that are referred to as the ENSO cycle, the atmospheric bridge, the Kuroshio Extension, and the Aleutian low.

ENSO has been correlated with the PDO in several ways. If PDO and ENSO are in phase, the PDO can be constructive, causing a positive feedback with the ENSO cycle, while if they are out of phase, the PDO can act destructively on ENSO (Kwon et al. 2012). In the proposed cycle, ENSO also has an effect on the PDO cycle and can possibly lead to a change of the PDO phase. The eastern Pacific ENSO has shown the strongest correlation with the PDO phase changes. (DiLorenzo et al. 2010). This type

of ENSO causes warm anomalies in SSTs off the coast of western South America and enhanced precipitation, with cooler temperatures in the western Pacific and a decrease in precipitation, leading to drought conditions in eastern Asia (Alexander et al. 2002).

The changes in sea surface temperature from the ENSO cycle alter the atmospheric circulation, creating what is referred to as an atmospheric bridge. The atmospheric bridge theory is a component of the proposed cycle. The warmer SSTs in the tropics lead to an enhanced Hadley cell circulation, with a larger air mass ascending at the equator and a descending counterpart in the subtropics (Yeo et al. 2012). ENSO is also a heat source and produces Rossby waves that propagate to the extratropics (Yeo et al. 2012). The main energy budget factors affected by the atmospheric bridge are the net surface heat flux, the entrainment heat flux and the Ekman transport. These affect the budget of the North Pacific, the net heat flux having the dominating effect on forcing North Pacific SSTs (Alexander et al. 2002). The atmospheric bridge can also influence storm tracks in the Pacific, since ENSO brings more moisture to the atmosphere as well.

Another product of this increased moisture and change in temperature in the North Pacific is an intensification and eastward shift of the Aleutian low (Yeo et al. 2012). The enhancement of the descending component of the Hadley cell circulation from ENSO aids in the shifting and intensifying of the Aleutian low (Yeo et al. 2012). This forces more local features in the North Pacific, with the enhanced cyclonic motion in the atmosphere increasing winds and bringing cool, dry air to the central North Pacific, and causing negative SST anomalies and heat flux. Warm, moist air is brought by winds up the western coast of North America, causing positive anomalies in the net heat flux and SSTs (Yu & Kim 2011).

Another component to the variability in the North Pacific ocean is the Kuroshio Extension, which is located off the coast of Japan at 35°N and 140°E. This is a section of the Kuroshio current, the western boundary current in the Pacific, which forms a variable boundary between the warm and cooler regions of the northern Pacific. This current is the main modulator of the western Pacific variation and can affect changes to the heat transport in the Pacific. Its importance to the PDO is on decadal time scales (Schneider & Cornuelle 2005). This area has 2 different fluctuations that occur, the jet placement and strength (Taguchi et al. 2007). The sea surface height (SSH) field for this region is usually used as a mechanism to monitor the oscillations. The first EOF of these SSH fields yields a decadal fluctuation that shows a meridional profile with a peak in SSH at 35°N. This indicates a stronger jet with a southern adjustment (Taguchi et al. 2007). These anomalies are a proposed product of baroclinic Rossby waves propagating westward due to changes in the wind stress curl field (Taguchi et al. 2007). The changes from ENSO to the Hadley cell can cause changes to the wind fields, resulting in these Rossby waves (Wang, Wu & Fu 2000). Changes in the Kuroshio Extension can also be a lagged response to PDO phase changes (Qiu 2003). The influence of the Kuroshio Extension can be extended to the eastern Pacific by the increases in zonal advection, which enhances eastward flow and warms regions east of the date line (Schneider & Cornuelle 2005).

Many studies have been conducted using both modeled and observational data to understand the timing between the components of this cycle. ENSO is the initial forcing, which causes changes in the rest of the component fields. The ENSO signals are usually strongest during the winter months. Changes in the Aleutian Low have been seen as soon as one year after the ENSO signal is well established (Alexander

2002). Influences of the ENSO cycle and Aleutian Low can both contribute to shifts in the jet of the Kuroshio Extension. ENSO leads the Kuroshio Extension shift by 4 to 5 years, while the SLP anomalies lead by 3 years (Park et al. 2002, Deser 2011). The north Pacific SST anomalies, the PDO phase change, lags the ENSO change by 12 to 18 months in most studies (Alexander 2002). The lag period between the SLP and north Pacific SST anomalies tends to be shorter, about 6 months, due to the proximity of the phenomenon (Furtado 2011).

1.2.3 PDO in Models

The PDO has been studied using many different climate models, both current and past generations. It is well represented in some of the earlier models, such as the Community Climate System Model ver. 2.0. The PDO anomaly pattern is seen on a sixteen year variation in CCSM2.0, with some of the atmospheric processes related to the variation not replicated as well (Kwon & Deser 2006).

Many models from the Climate Model Intercomparison Project 3 (CMIP3) were used to analyze the PDO and possible atmospheric and oceanic teleconnections. Several studies have shown that many of the models have a high reproducibility of the spatial patterns of the PDO (Oshima & Tanimoto 2009). However, the magnitude of the anomalies is either underestimated or spatially displaced in many of the models (Stoner et al 2009). Some showed stronger anomalies and larger effects from atmospheric forcings on the oceanic patterns (Furtado et al 2011). However, there were some issues with these models that limited the replication of the PDO. In particular, the CCSM3.0 did not represent the ENSO cycle well. The ENSO events were too frequent, averaging every 2 years instead a range from 3 to 7 years. This affected how the PDO was represented and how it correlated with the ENSO cycle in

the modeled data (Park et al. 2013). Also, most of the oceanic components in the global climate models do not correctly simulate subsurface dynamics entirely, which limits the effect of the KOE on the PDO cycle (Park et al. 2013).

The CMIP3 generation of models was also used by several studies to replicate and test the relationship between the tropical and north Pacific. With the effect of the ENSO cycle removed in the models, a PDO signal still exists (Pierce et al. 2001). In one study using a climate system forecast model (CFS ver. 1.0) the PDO becomes the second EOF pattern in the north Pacific SST field without the effect of ENSO (Wang et al 2012). The PDO exists in the model, but the signal is not as strong. While the PDO is heavily influenced by ENSO activity, it is not only a teleconnected response to ENSO (Zhong et al 2008). Without the presence of ENSO, surface wind features were found to be dominant in forcing oceanic patterns in the north Pacific (Wang et al. 2012). ENSO has also been used in attempts to predict PDO variability. In a study using observations and the HadCM3 model, PDO forecasts needed initial conditions for each year, since there are several forcings involved in the PDO cycle. ENSO only proved a reliable source for predictability for a three year forecast (Leinert & Doblas-Reyes 2013).

With improvements in GCMs, there has been more confidence in the ability to replicate the PDO and study the possible mechanisms behind its cycle. In CCSM ver. 4.0, the ENSO cycle was drastically improved to correct for the overestimation of the frequency of events in the model. The ENSO and PDO spatial and temporal patterns are realistically replicated (Deser et al 2011). The correlations between these two variability features is also improved, though the connection is still weaker than that found in observations (Landrum et al. 2013). Other possible climatic links to the PDO

are represented as well. SLP anomalies in the north Pacific are consistent with those indicative of the Aleutian Low variation (Deser et al 2011).

1.2.4 Model History

The Community Climate System Models are coupled global climate models which are developed at the National Center for Atmospheric Research (Vertenstein). This set of climate models were born out of the NCAR Climate and Global Dynamics Division and began as a three-dimensional atmospheric model, the Community Climate Model (CCM0). It was based on spectral models from Australia and the European Center for Medium range Weather Forecasting (ECMWF). With CCM3.0, many important changes were made so the atmospheric model would be more suitable for coupling to other component models, such as ocean and ice models. This objective was fully achieved with the release of CAM3.0, Community Atmospheric Model 3.0, identifying the model as a larger part of a coupled system, CCSM3.0 (Neale et al 2010). Earlier versions of the CCSM projects were used mostly to test combinations of different atmospheric, land and ocean models (Buja & Craig 2002). With the release of CCSM4.0, which will be used for this study, many of the components have been updated to include more realistic parameterizations and processes.

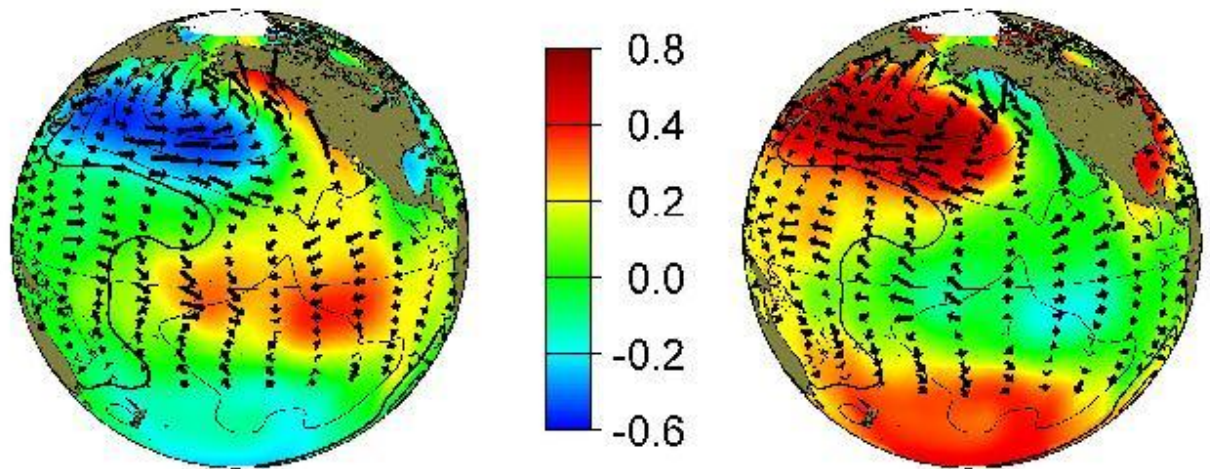


Figure 1.1 The Pacific Decadal Oscillation Phases: The typical PDO cool (left) and warm (right) phase patterns are displayed. The colors indicate SST, in °C, contours outline the SLP and surface wind stress is denoted by the arrows (JIASO).

Chapter 2

METHODS

2.1 Model Description

The data for this study come from the Community Climate System Model 4.0 (CCSM4.0). This is the fourth version of the fully coupled general circulation model (GCM) produced by the National Center for Atmospheric Research (NCAR). The model is run on both a 1° and 2° grid cell size, with varying input parameters involving different carbon emission scenarios (Gent 2011). The model has 5 main components: the atmospheric model, the land cover model, the ocean model, the sea ice model and the coupler.

2.2 Model Components

2.2.1 Atmospheric Model

The Community Atmospheric Model 4.0 (CAM4.0) is the 6th generation of version of the atmospheric model from NCAR. It has a horizontal latitude/longitude grid and a vertical grid with 26 levels (Gent 2011).

This model uses a Lin-Hood finite-volume dynamical core, as opposed to the previous spectral core (Gent 2011). The finite volume core integrates differences over grid boxes to maintain the governing equations and laws. The governing equations for the hydrostatic atmosphere in this model are the hydrostatic balance equation, the conservation of mass, the momentum equations and the first law of thermodynamics

(Appendix A) (Neale 2010). There is also an option for a spectral element dynamical core.

The vertical coordinate system in this model uses terrain-following quasi-Lagrangian coordinate, which functions exactly like the η coordinate used in previous versions of CAM (Equation 2.1). A , B , P_0 are constants and P_s is the current surface pressure (McCaa 2004).

(Equation 2.1)
$$p_{(i,j,k)} = A_k P_0 + B_k P_s(i,j)$$

The parameterization package in this model is the sum of four main components: precipitation processes, clouds and radiation, the surface model and turbulent mixing. These components can be further broken down into separate variables, while the temperature is determined by changes in dry static energy (Neale 2010). The deep convection processes and cloud modeling were significantly improved in this version. The momentum equations include the deep convection and the plume calculation uses a dilute approximation, which has lessened the frequency but increased the intensity of deep convection. The cloud modifications have reduced the amount of wintertime low clouds in the Arctic (Gent 2011). The deep convection modifications aided in a better reproduction of ENSO, which is important to the cycle and simulation of the PDO (Neale 2010).

2.2.2 Land Model

The land model used in this GCM is the Community Land Model 4.0 (CLM4.0), which parameterizes land surface processes. Each grid cell can have

several different land types, known as land units, which in turn can be divided into different types of land coverage including different vegetation type (Oleson 2010). The model has been improved to include several biogeophysical processes, which will interact with the atmospheric model and hydrological processes. There is also an option for dynamic vegetation, so that the land types can evolve with the changes in the climate (Oleson 2010). The dynamic vegetation option was not utilized during the run used in this study.

2.2.3 Ocean Model

The ocean model used in CCSM4 is the Parallel Ocean Program version 2 (POP2). The governing, primitive equations are the momentum equations, continuity equation, hydrostatic equation, equation of state and tracer transport, which are all listed in Appendix A (Smith 2010). These equations are solved in the general orthogonal coordinates with hydrostatic and Boussinesq approximations. The barotropic equation uses a surface pressure formulation, which allows for changes in surface layer thickness (Los Alamos 2010).

The ocean model uses a tripole grid with spherical coordinates in the Southern Hemisphere and slightly different coordinates in the Northern Hemisphere. The North Pole is displaced so that it occurs over Greenland, the zonal resolution remains constant at 1.125° and the meridional resolution fluctuates between 0.27° to 0.64° to account for the spherical shape. The horizontal grid is two dimensional (Danabasoglu 2006). In the vertical grid, there is a 10 meter resolution from the surface to 160 meter depth. After this upper ocean, the resolution is 250 meter until 3500 meter depth, below which variables remain constant (Danabasoglu 2012).

2.2.4 Sea Ice Model

The sea ice model in CCSM4 is the Los Alamos sea ice model, CICE, which was designed to work with the POP2 model. The model has several components which account for the growth rates of snow and ice, incorporation of snowfall, velocity of the ice pack and ice volume and thickness. These parameters are weighted by the fractional ice coverage of the grid cells and are then passed through the coupler to the other components of the global model (Hunke 2013). A more detailed description of the model can be found on the Climate, Ocean and Sea Ice Modeling Group website from Los Alamos National Laboratory at oceans11.lanl.gov.

2.2.5 Coupler

CPL7 is the new coupling component used by CCSM4. The components are run separately and then coupled so that incorrect forcings in one component are not compensated by another component. The only parameters that can be altered when the components are coupled are the sea ice albedos and the relative humidity threshold above which low clouds are formed (Gent 2011). The atmosphere, land and sea ice components are coupled every half hour to better imitate the diurnal cycle, while the ocean component is coupled only once to a few times a day. The less frequent coupling of the ocean model allows for the lag in response to ocean forcings seen in nature (Craig). There is an option to tightly couple the ocean model without any lags, though it is not often used and was not used for this run (Craig).

2.3 Run Specifications

The data selected for this study were from the pre-industrial control run due to the focus on the replication and cycle of the PDO. The pre-industrial run used the 1850 parameter values (Gent 2011). This run was performed from 9/3/2009 to

1/3/2010 and the data were released on 5/1/2011 from NCAR. The run included 1300 years of monthly data values on a $.9^{\circ} \times 1.25^{\circ}$ grid. The data from years 1 through 200 were used for this study.

Chapter 3

RESULTS

3.1 EOF Analysis

To understand if the model is correctly replicating the pattern of the PDO as seen in observations, empirical orthogonal function (EOF) analysis is used to extract the spatial and temporal patterns of the longterm oscillations in the Northern Pacific SST field. The EOF analysis uses a correlation or covariance matrix to compute the eigenvectors and eigenvalues of a dataset. This method, also known as principal components analysis, produces a set of uncorrelated vectors that represent linear combinations of the original variables and are ordered by the amount of the data each explains. A large amount of the variance is explained by the first few eigenvectors. The dataset must be spatially weighted and reduced to anomalies before the EOF analysis can be performed. For this study, all correlation matrices were used to calculate the EOFs to minimize extreme values, except for the SLP field, for which a covariance matrix was used.

The data were spatially weighted by the cosine of the latitude in order to reduce the influence of smaller grid boxes that lie closer to the poles. The mean of the field was removed at each grid point, as well as the seasonal cycle and any linear trends within the dataset.

3.1.1 Spatial Representation

The first EOF of the modeled SST field from 20° to 70°N and 120°E to 100°W shows positive, warm anomalies off the western North American coast and cooler anomalies in the central Pacific, extending to Japan and Eastern Asia (Figure 3.1). This mimics the pattern outlined by Mantua, which has been seen in observations and called the positive phase of the PDO (1997). The literature shows a range of 22-27% of the variance explained by the first EOF of the North Pacific SSTs (Deser 2012, Park 2012). The modeled output from this study showed 23% of the variance is explained, which is within the range of other studies. The magnitude of the temperature differences for the warm and cold pools for the PDO are also replicated well, ranging from -0.8 to 0.6°C in anomalies. This is also similar to observations seen (Park 2012).

The spatial pattern of the modeled SST first EOF is directly compared to the first EOF from SST observational data in Figure 3.2. The observational data were obtained from NASA's Goddard Institute for Space Studies (GISS) Surface Temperature Analysis. It is a dataset of surface temperature anomalies on a 2° by 2° grid. The modeled spatial field is subtracted from the observational field (Figure 3.2c). The EOFs display opposing phases, so the absolute values are taken of each field before they are subtracted. The modeled data show a higher variance explained by the first EOF than the observational dataset, though both are within 3% of each other. The differences show slightly higher values off the coast of western North America and in the central pool, with a band of slightly lower values between the two higher bands.

The first EOF of the SLP field, following the same bounds as the SST field, represents the Aleutian Low index, which is also shown in Fig. 3.1b. Observations show a similar pattern centering off the coast of Japan. The maximum low pressure

center for observations lies around 45°N latitude and 165°W longitude, while the spatial pattern from the modeled output has a slightly higher center, around 55°N latitude (Park 2012). Other studies have shown this northern bias in many models, specifically the previous CCSM 3.0 model. The model does show 38% of the variance is explained by this pattern, while observations typically show 36% (Park 2012).

The first EOF of the SSH field was calculated from 30 to 45°N latitude and 140 to 170°E longitude (Figure 3.1c). The SSH field pattern shows negative SSH anomalies along the jet between 35-40°N latitude. Observations show similar EOF patterns, with the extreme closer to the 35°N latitude line. The EOF explains 41.5% of variance in the SSH field in observations, while this modeled output has a higher variance explained, approximately 46%.

The tropical SST field was examined to represent the component of the ENSO cycle. It was analyzed by EOF analysis from 20°S to 20°N and 120°E to 100°W. The first EOF shows a cold anomaly in along the equator with warm anomalies in the subtropics, which is indicative of a La Nina pattern (Figure 3.1d). This pattern explains 61.2% of the variance in the modeled dataset. Other studies have shown lower variance explained percentages (Lian & Chen 2012); however their area analyzed is larger than the area used in this study.

The zonal wind stress field was also analyzed through the EOF method over the same bounds as the SLP and north Pacific SST fields (Figure 3.1e). The zonal wind stress indicates the easterly or westerly movement of ocean waters forced by the wind field. The first EOF of the zonal wind stress field shows an easterly enhancement from the Kuroshio Extension toward the central north Pacific. There is also a slight

increase in wind stress in the subtropics westward, toward the Kuroshio Extension. This pattern explains 21% of the variance in the dataset.

3.1.2 Temporal Patterns

The yearly averages of the monthly EOF time series are calculated from June to the following May, centering on the winter months, when the PDO is most active (Figure 3.3). Each of the fields shows great variation over the 200 year period, with periods of negative and positive indices. The SSH field has the greatest consistency in longer positive or negative anomaly time periods. The north Pacific SST field also has longer periods of negative or positive anomalies, while the tropical SST field has much more frequent fluctuations.

3.2 Time Series Analysis

Time series analysis was used to examine the spectral densities of the each of the derived yearly time series. Spectral density plots look at the time series from a frequency standpoint, reducing the time series to a series of frequencies and their respective strengths. This is achieved by estimating the coefficients of the Fourier series of the time series, which transforms the data from the time domain into the frequency domain. The NCL function, `specx_anal`, calculates the spectra of a time series. The function returns attributes of frequency and the power of the series at each frequency.

The spectral densities of the first EOFs of all the analyzed fields are shown in Figure 3.4. The time series for the SLP field (Figure 3.4a) shows several spikes in power between the 4 and 8 year frequencies. There are also smaller power spikes at the 10 to 15 year frequencies. This indicates that there are strong 4 to 8 year signals in

the northern Pacific SLP, with lower power signals at the 10 to 15 year frequencies. The spectra of the first EOF of the northern Pacific SST field (Figure 3.4b) also shows high power at higher frequencies, from 4 to 8 years, with the highest power at 7 years. There are also several lower power frequencies between 12 to 16 years. The SSH field over the Kuroshio Extension (Figure 3.4c) has equal power signals in the higher frequencies of 4 to 8 years and lower frequencies of 10 to 15 years. The tropical SST field (Figure 3.4d) shows the highest power signal at a frequency of 4 years. The signals are also highest at the 3 to 5 year range for the zonal wind stress field, with a smaller peak at the 12.5 year frequency. The north Pacific SST, SSH and tropical SST field all show much higher power signals than those of the SLP and zonal wind stress fields.

3.3 Filtering

The higher frequency variations in the modeled output fields interfere with the lags between the cycle components, since the signals of the PDO are on a decadal scale. Applying a filter to the data isolates the longer oscillations within the Pacific Ocean fields that could force the changes in the northern Pacific SSTs. For this study, a lowpass Lanczos filter was used which utilizes the sinc function to isolate the lower frequency signals after the cutoff frequency. The Lanczos filter minimizes leakage of the signal and the Gibbs phenomenon at the cutoff frequency as compared to the traditional box filter. The Gibbs phenomenon is result of the discontinuity when using a filter at the transition between the signal and the cutoff frequency, leading to large oscillations at the discontinuity. This is smoothed by the use of the sinc function which is not as fast of a transition as a box filter (Duchon 1979). Further explanation of the details of the Lanczos filter can be found in Duchon (1979). For this study, the

cut off frequency, f_c , was set at $1/120$, a frequency of 120 months, or 10 years. The amount of weights used was 61. The weights for the Lanczos filter are determined by Equation 3.1, where the number of weights is $2n - 1$.

(Equation 3.1)

$$\omega_k = \left(\frac{\sin 2\pi f_c k}{\pi k} \right) \left(\frac{\sin \frac{\pi k}{n}}{\pi k n} \right)$$

The filter does cause loss of data at the ends of the time series. Half the number of weights is the number of data points lost on each end. However, the more weights used, the better the filter. This filter caused a loss of 2.5 years on each end of the time series. The higher frequency signals are not removed completely; however, they are minimized to better visualize the lower frequency signals. The increase of weights would reduce these signals close to 0, but to retain as much data as possible, it is only necessary to reduce their influence to detect the lower frequency signals.

3.3.1 Filtered Results

The filtered spatial patterns of the first EOFs of each field do not differ greatly from the original outcomes. A notable difference is the change in the northern SST field. The pattern has switched from resembling a positive phase PDO to a negative phase PDO, with a warm pool in the central north Pacific and a cold pool off the western coast of North America. The tropical SST field was not filtered since it should represent the ENSO pattern, which occurs on a 3 to 8 year time scale.

The yearly averaged time series for each of the fields shows a much smoother, consistent pattern (Figure 3.5). The decadal patterns within the output are much more pronounced and the positive and negative anomaly periods are discernible. The

tropical SST field remains unfiltered, so the shorter time period fluctuations of the ENSO cycle are visible.

The filtered spectral densities, shown in Figure 3.6, do show significant change from the unfiltered versions. In each of the fields, the higher power signals at the 4 to 8 year range have been decreased, while now the lower frequency signals, in the 10 to 15 year range, are dominant. The SLP field shows high power at the 15 and 25 year frequencies. The north Pacific SST spectra shows a large peak at the 20 to 30 year frequency, with other peaks at the 12 to 18 year range. The SSH field has a high power frequency at 15 years. The zonal wind stress field displays a large signal at the 12.5 year frequency, with slightly lower powered signal at the 15 year frequency.

3.4 Lag Correlations

To determine how the components of the cycle interact with one another, lag correlations are computed between the fields. This method compares two time series by increasing the time step of one time series and computing the cross correlation between the two series at each lag (Equation 3.2). It shows how one time series leads or lags against another time series. Each dataset was lagged at a maximum of 200 months versus the other. For a correlation to be statistically significant at the .01 level for these datasets, it had to exceed 0.181.

(Equation 3.2)

$$c(k) = \frac{(\sum_{j=1}^N (x(t) - \bar{x})(y(k+j) - \bar{y}))}{(std(x) * std(y))}$$

Some of the fields were limited in their spatial ranges to limit the possibility of confounding signals. The North Pacific SST and zonal wind stress fields were limited to 20 to 60°N latitude by 120°E to 100°W longitude to remove any extreme values

near the poles. The SLP field was restrained to 40 to 60°N latitude by 180°E to 140°W longitude to isolate the Aleutian Low signal.

3.4.1 North Pacific SST Lag Correlations

The time series of the first EOF of the north Pacific SST field, the representation of the PDO, is lagged against each of the other components. As shown in Figure 3.7, the SST field was lagged over a period of 200 months. The lag correlations with the SLP field show a large negative correlation at lag 0, decreasing until a maximum of -0.81 at 8 months, where the correlation then increases until it is close to 0. The SSH lag correlation shows a value close to 0 at lag 0, with a decrease until 60 months, or 5 years. The maximum correlation is -0.3. The tropical SST lag correlations indicates a positive correlation at lag 0 and continues until 8 months, where it maximizes at 0.22. The correlation then decreases until it hits a minimum correlation of 0.18 at 36 months, or 3 years. In the lag correlations with the zonal wind stress, there is an initial positive correlation with the north Pacific SST time series until 1 year, at which the correlation maximizes at 0.5. It then decreases until 0 at 48 months, or 4 years.

3.4.2 Lag Correlations between Other Components

To map out the cycle, it is necessary to investigate the lag and lead relationships between the other components. The SLP time series is lagged against the SSH time series, as seen in Figure 3.8a. There is a maximum correlation of 0.3 between these time series at 4.4 years. The lag correlations between zonal wind stress and SLP (Figure 3.8b) show a maximum of -0.6 at a lag of 6 months. The SLP time

series initially shows a correlation of -0.25 with the tropical SST time series (Figure 3.8c) at 3 months. There is a second maximum of 0.25 at a lag of 2.5 years.

Lag correlations between the zonal wind stress and the SSH time series (Figure 3.8d) indicate a minimum correlation of -0.46 at the lag of 1 year. There is a positive maximum of 0.18 at 8.4 years. The tropical SST and SSH time series (Figure 3.8e) show an maximum correlation of -0.22 at a lag of 6 months. The last lag correlation, tropical SST and zonal wind stress (Figure 3.8f), indicate an initial maximum correlation of 0.5 at lag 0 and a minimum correlation of -0.39 at 2.2 years.

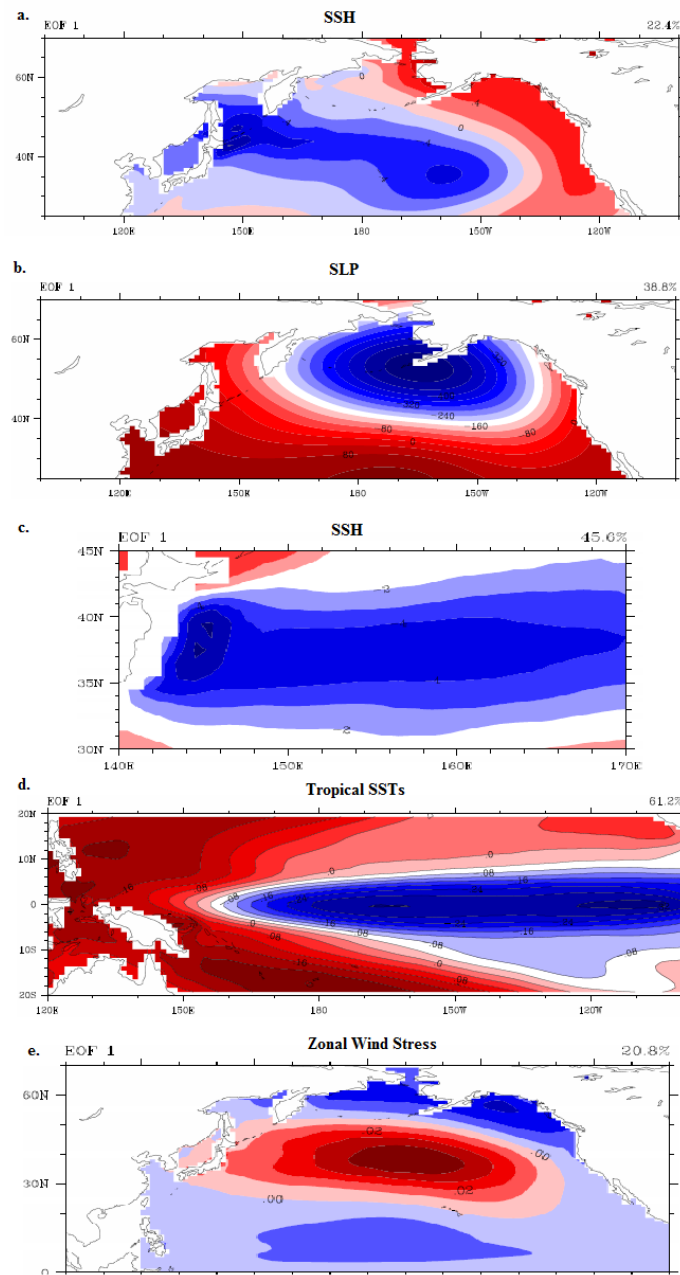


Figure 3.1 First EOFs of Variable Fields: The normalized PC time series from the first EOF of each variable regressed onto respective anomaly fields. a. shows the SST anomalies in units of $^{\circ}\text{C}$, b. is the SLP anomalies in Pa, c. is the SSH anomalies in units of cm, d. is the tropical SST anomalies in $^{\circ}\text{C}$ and e. is the zonal wind stress component anomalies in N/m^2 .

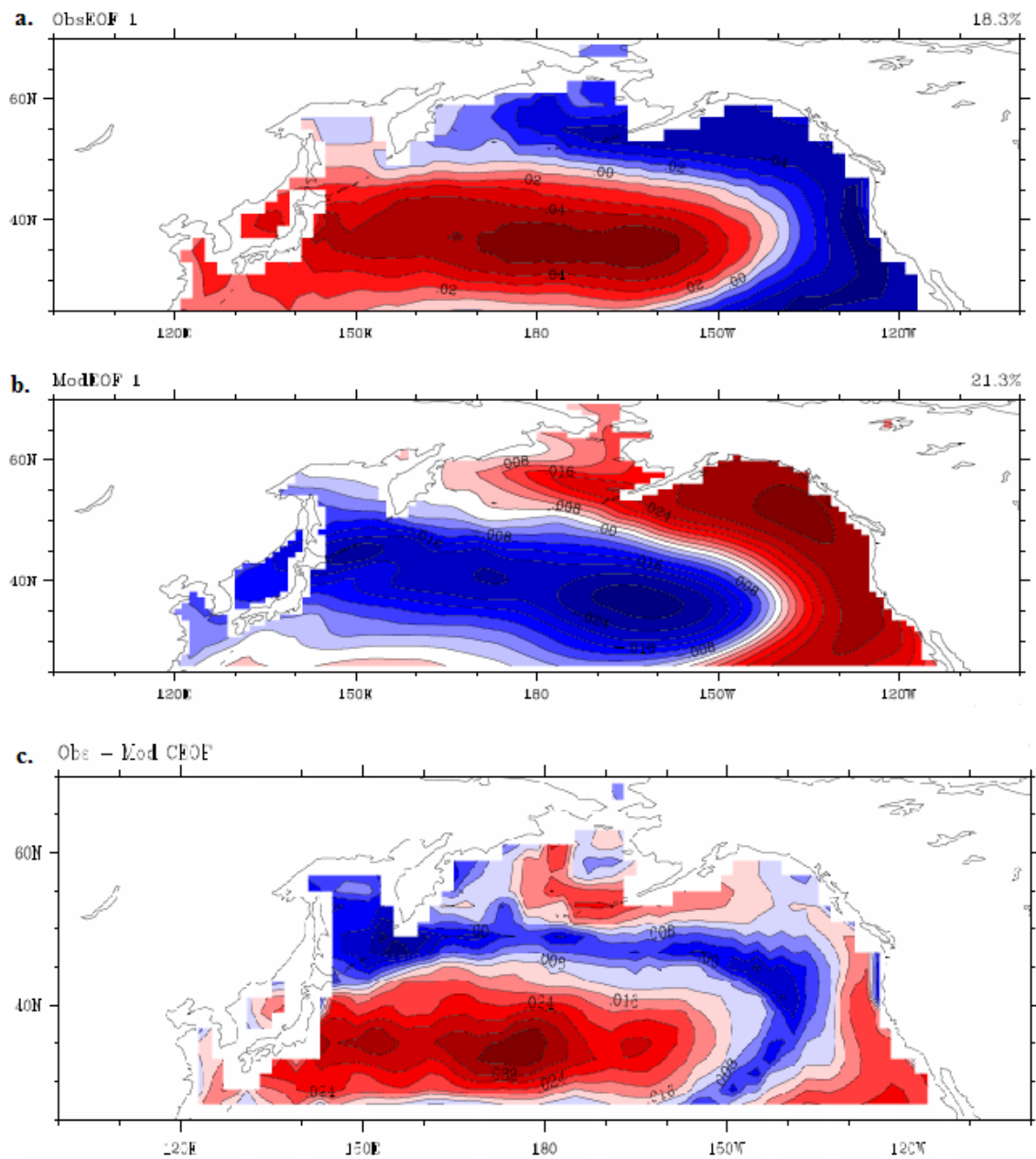


Figure 3.2 Modeled EOF vs. Observational EOF: The first EOF of the a. modeled SST field is compared to b. observational data. C. is the absolute value of the first EOF of the modeled data subtracted from the first EOF of the observational data.

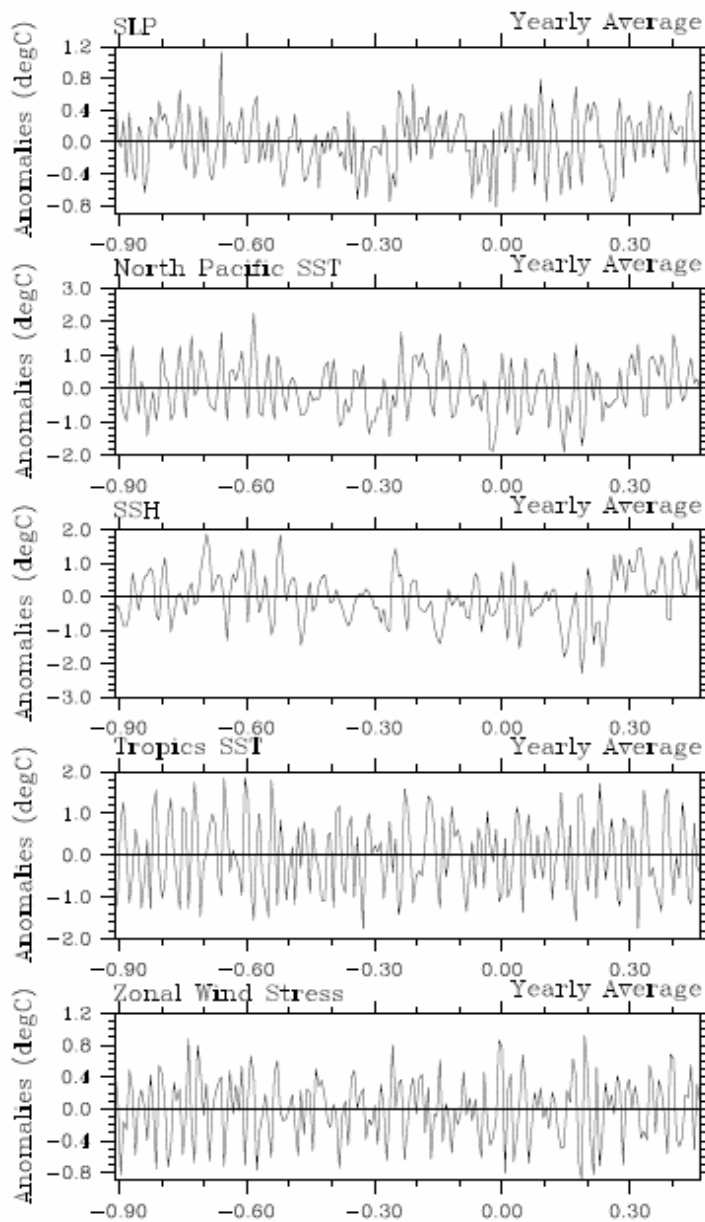


Figure 3.3 Yearly Average Anomalies: The yearly averaged anomalies, centered on the winter season, are displayed for each of the first EOFs of each analyzed field. A. shows a yearly average for the SLP field, b. the North Pacific SST field and c. the SSH field along the Kuroshio Extension. D. shows the yearly average tropical Pacific SST field and e. is yearly average the zonal wind stress field.

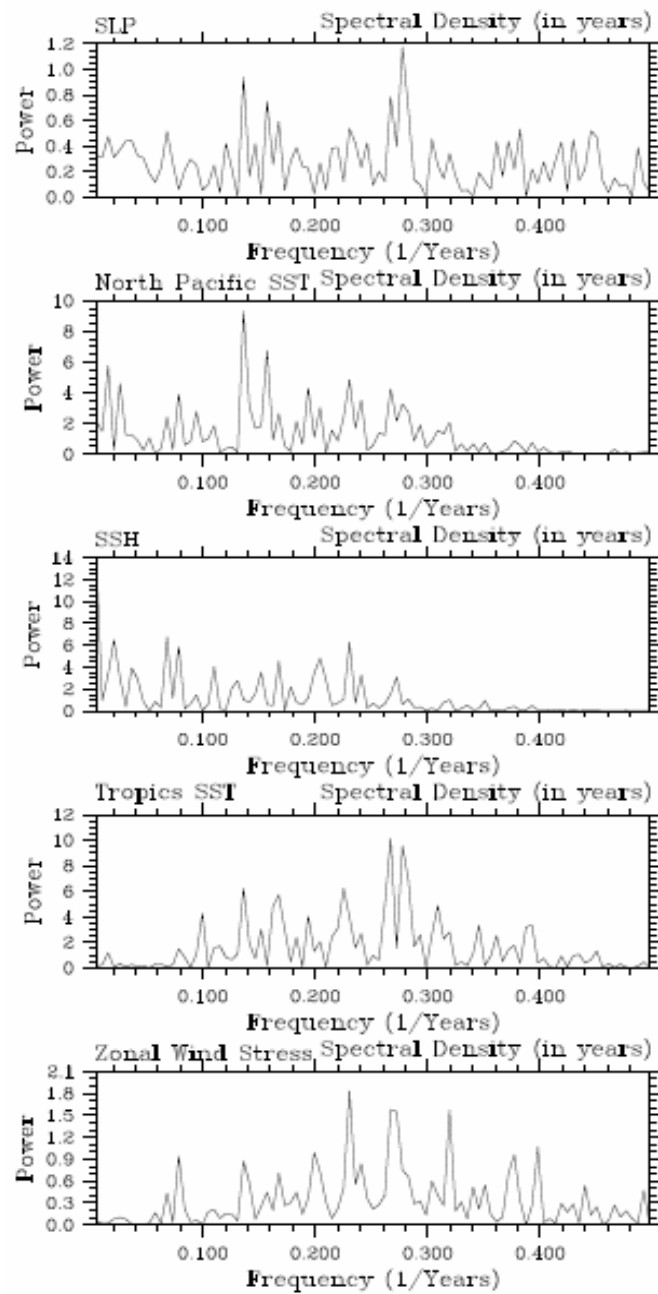


Figure 3.4 Spectral Densities of Variable Fields: The spectral densities are shown for the first EOF of each field by the frequency, in years, versus the power of the signals. The spectral density of the SLP field is shown in a., while b. shows the North Pacific SST special density and c. the SSH spectral density. D. shows the spectral density of the tropical Pacific SST field and e is the zonal wind stress spectral density.

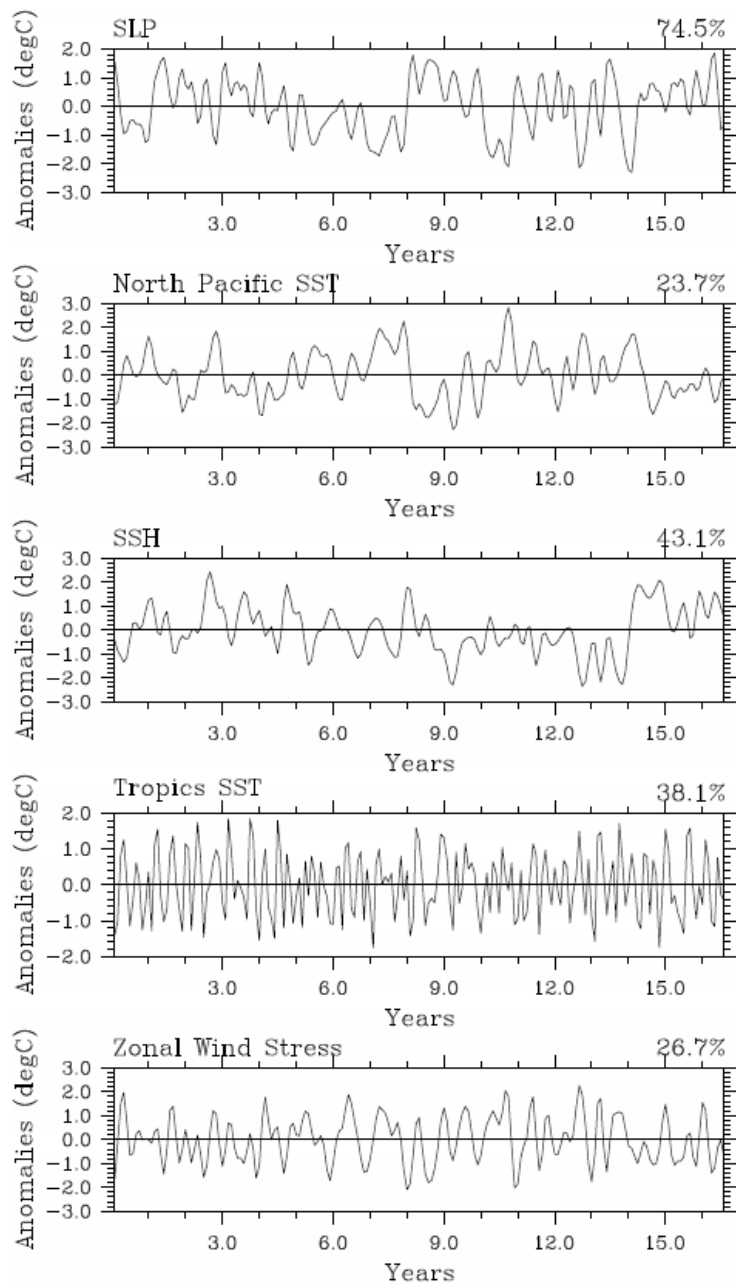


Figure 3.5 Filtered Yearly Average Anomalies: The yearly averaged anomalies from the time series of the first EOF of each field over the 200 year period are displayed. A low-pass filter has been applied to the a. SLP, b. North Pacific SST, c. SSH and e. zonal wind stress fields. The d. tropical Pacific SST field remains unfiltered.

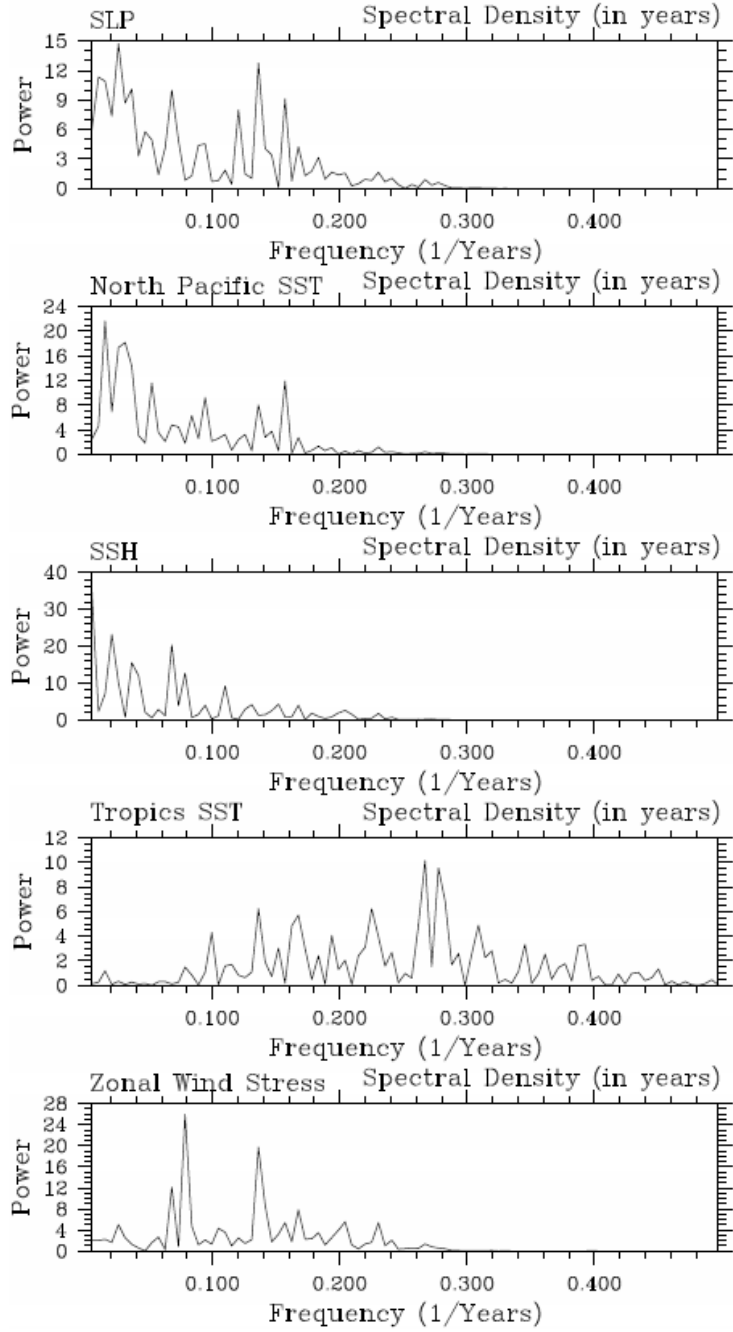


Figure 3.6 Filtered Spectral Densities of Variable Fields: The spectral density was calculated for time series of the first EOF of each field. A low pass filter has been applied to the a. SLP, b. North Pacific SST, c. SSH and e. zonal wind stress fields. The d. tropical Pacific SST field remains unfiltered.

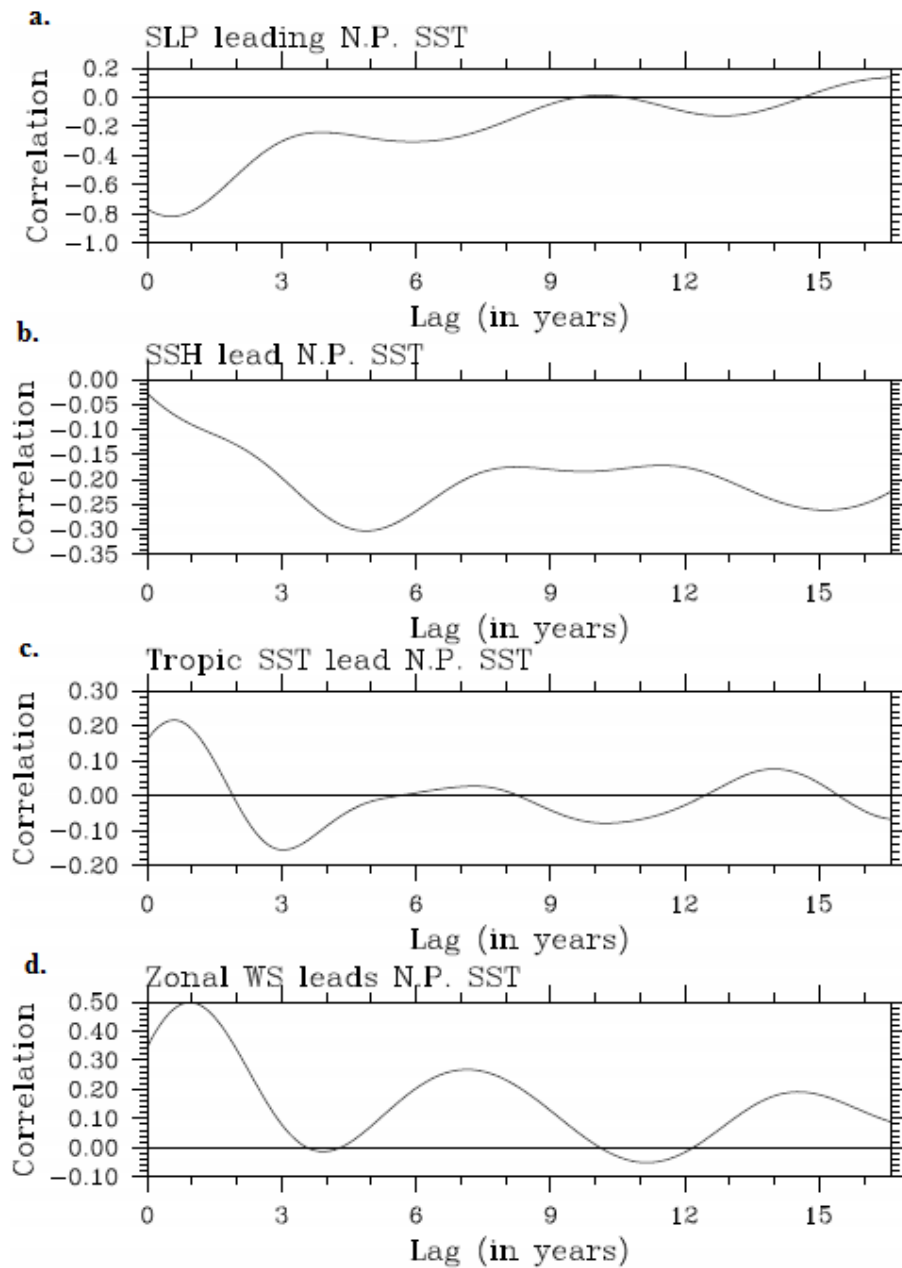


Figure 3.7 Lag Correlations with North Pacific SSTs: Lag Correlations were computed between the time series of first EOF of each of the components and the time series of the first EOF of the North Pacific (N.P.) SST. The lag refers to the years in which the N.P. SST time series lags the corresponding time series.

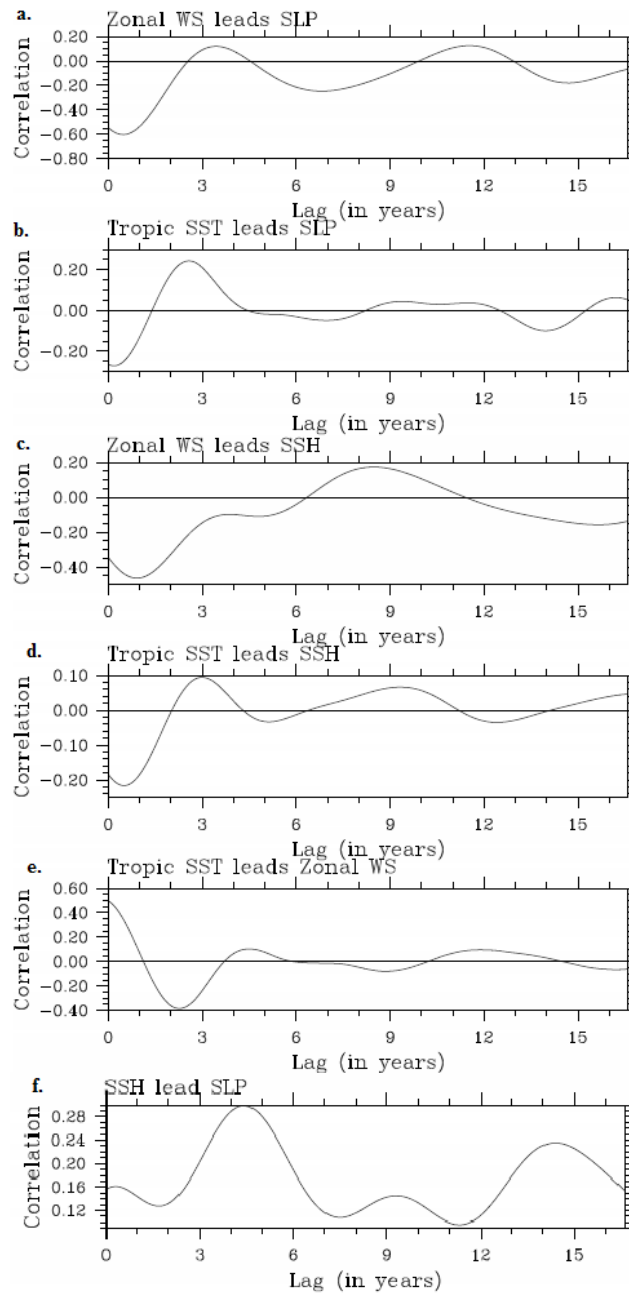


Figure 3.8: Lag Correlations between Other Variables: The time series of the first EOF of all components, excluding the N.P. SST field, were lagged against one another. a. and c. show the SLP field and SSH field lagging the zonal wind stress (WS) field respectively. b., d. and e. show the tropical SST field leading the SLP, SSH and zonal WS fields respectively. f. refers to the SSH field leading the SLP field.

Chapter 4

DISCUSSION AND CONCLUSIONS

4.1 EOF Spatial and Temporal Patterns

4.1.1 Representation and analysis

Model output from the CCSM4 pre-industrial control run shows clear representation of the PDO, both spatially and temporally. The comparison with the observational data shows that the positive areas are where the observational EOF has a higher value, while the negative areas are a higher anomaly in the modeled data. Figure 3.2c indicates that the observational data exhibit higher anomalies in the central Pacific and off the coast of Japan, as well as off Alaska and southern California. The modeled data has higher anomalies off the coast of Russia and toward the 150°W longitude line. Looking at the individual EOF patterns, the modeled EOF has a slightly higher focal point, around 45°N latitude for the western part of the PDO, while the observational data have a slightly lower focal point, around 40°N. The eastern portion of the PDO also extends further westward in the observational EOF than the modeled. Overall, the patterns show the horseshoe shaped pattern off the coast of North America and the central pool, as displayed in Figure 1.1.

4.2 Spectral Densities

The spectral density plots for each of the unfiltered time series shows both a lower 10 to 15 year frequency signal, as well as a higher frequency signal at 3 to 8 years. This higher frequency signal falls in the range of the observational time period of the ENSO cycle, while the lower frequency signal is in the range of the PDO

temporal signature. Since ENSO is part of the overall proposed forcing of the PDO, the indication that the ENSO cycle influences each of the components aids in understanding how ENSO acts as an initial forcing. The ENSO signal is strongest in the North Pacific SST time series, which helps support the atmospheric bridge theory which was earlier discussed (Yeo et al. 2012).

The filtered time series decreases the possible ENSO signal to better isolate the lower frequency PDO-like signal. Once filtered, the SLP, North Pacific SST and SSH time series have large peaks at lower 20 to 30 year frequencies, as well as peaks at the 12 to 18 year frequencies. This may indicate a longer term variation than the PDO, or perhaps a signal from a full cycle of both phases of the PDO. However, the spectral densities all show a signal similar to that of the PDO signal seen in observations. The zonal wind stress series (Figure 3.6e) has an isolated peak at the 12.5 year frequency. The longer period signal that affected most of the other fields does not seem to have the same effect on the zonal wind stress field.

4.3 Lag Correlations

4.3.1 Connections with the North Pacific SST field

The lag correlation plots clarify the order in which the physical components influence one another. All the correlations discussed exceeded the threshold for significance at the .01 level. The north Pacific SST time series lagged against each of the other components shows the order in which they force the SST changes. Since the filtered EOF pattern for the north Pacific SST field displays a negative phase of the PDO, negative lagged correlations indicate a correlation with the positive phase, while positive correlations show the field is correlated with the negative phase at that lag.

The first component of the proposed cycle is a forcing from the ENSO cycle. The lag correlations show two correlations of larger magnitude, one at six months and one at 3 years. The first positive correlation, at a lag of 6 months, indicates that the negative phase correlates with the negative tropical SST field phase, or that the two fields are in phase with one another. As time progresses, there is another correlation which is negative at a lag of 3 years, which indicates that the two EOF patterns are out of phase with one another. The magnitude of the correlations between the tropical SST field and the north Pacific SST field are not as high as those seen in observations, indicating that the tropical SST field may not be as large of a forcing on the north Pacific SST field in this model. The lag between these two changes is also longer than seen in previous studies (Alexander 2002).

The first EOF of the SSH field, which is used as an indicator for heat transport from the Kuroshio Extension, show a negative correlation at a lag of 5 years with the first EOF of north Pacific SST. This indicates that the first EOF of the SSH field would correlate with the positive phase of the PDO, or the north Pacific SST field. The correlation between these two fields has a magnitude of 0.3, so the SSH field has a significant effect on the north Pacific SSTs in the model, though it is not the greatest forcing for the north Pacific. In past studies, the lag time between the components of the eastern Pacific and the western Pacific were similar to this, averaging 5 years (Park et al 2012). This result is consistent with that time period.

The zonal wind stress time series leads the north Pacific SST field by 1 year, with a correlation of 0.5. The positive correlation indicates the negative PDO phase lags the first EOF of zonal wind stress by 1 year. This is the second highest correlation between the north Pacific SSTs and any of the components, so the zonal wind stress

component is a significant forcing for the north Pacific SSTs in this model. Past studies also show that atmospheric changes tend to lead corresponding oceanic changes by one year (Deser 2011).

The SLP time series has a high negative correlation with the north Pacific SST series at lag 0, though the correlation increases in magnitude until a lag of 6 months. This negative correlation indicates that the SLP first EOF, which this study found as an intensification of the Aleutian Low, leads the positive phase of the first EOF of north Pacific SST field by 6 months. The magnitude of the correlation is the highest between these two fields, which designates the SLP field as a large forcing for the north Pacific SSTs in this model. The SLP forcing is the last component in the proposed cycle, so the shorter lead-lag period and the high correlation support the close connection between these two fields. This lag time is consistent with the 5 to 6 month time period seen in other models or in observational data (Furtado 2011).

4.3.2 Connections between other components

Since the proposed cycle includes several components, it is also important to understand how they correlate with one another. The first EOF of the tropical SST field has a high positive correlation with the zonal wind stress at lag 0, and a high negative correlation at a lag of 2.2 years. Since the ENSO cycle directly affects the Hadley cell circulation, the close connection between these two fields can be explained by ENSO affecting atmospheric conditions. The two high negative and positive correlations also indicates that the zonal wind stress EOF pattern is a product of both the positive EOF pattern of the tropical SSTs, which is similar to that of La Nina, and the El Nino negative phase. The first EOF of the tropical SST field leads the SSH EOF by 6 months, with a relatively high negative correlation of -0.22. The

negative El Nino like phase correlates with the changes in the Kuroshio Extension in this model, a theory which has been supported by many studies, both observational and modeled, which were discussed earlier. The EOF of the tropical SST field was correlated with the final component, SLP, which had two maximum correlations, one negative and one positive. The initial negative correlation at a lag of 4 months is most likely due to the effect of the El Nino-like pattern in the tropical Pacific causing changes to the atmospheric patterns and intensifying the Aleutian Low. This is a slightly shorter time period that was seen in previous studies which show a year lag (Alexander 2002). The later, slightly lower positive correlation at a lag of 3 years could result from the changes induced by the opposing pattern in the tropical Pacific on the atmosphere.

The first EOF of the zonal wind shear field has a high negative correlation of -0.6 with the first EOF of the SLP field at a lag of 6 months. The small lag between the patterns in these fields is most likely since they are both atmospheric mechanisms. The zonal wind stress EOF leads the SSH first EOF by 1 year, with a high negative correlation of -0.45. Zonal wind stress may be an indicator of the Rossby waves that are thought to induce changes to the Kuroshio Extension, as well as the connection between the Kuroshio Extension and the central north Pacific SST field. The negative correlation may be due to the first EOF pattern of the zonal wind stress causing an enhancement of wind stress westerly instead of easterly from influences of El Nino to cause changes to the Kuroshio Extension. The smaller positive correlation at a lag of 8 years could indicate the zonal wind stress field connecting changes in the Kuroshio Extension to the central north Pacific SSTs with the easterly enhancement of wind stress. The patterns in this study are not entirely consistent with previous studies,

which show wind stress anomalies leading those in the Kuroshio Extension by 3 years (Deser 2011). The lead-lag relationship between the SSH and SLP fields shows a lag of 4.5 for the SLP field against the SSH field. Since the SLP pattern is mostly concentrated in the eastern Pacific and the SSH pattern is a western Pacific phenomenon, the long lag between the two is most likely due to the slower heat transport in the ocean. The SLP anomalies have been shown to lead the SSH anomalies by 3 to 5 years in past studies (Deser 2011, Park et al 2012). The lead-lag relationship in this study may be symmetric about lag 0, which would follow the past studies' patterns.

4.4 Conclusions

The spatial and temporal representations of the components of the proposed cycle in this model are similar to those of observations, which indicates that the PDO is represented in this model and the mechanisms forcing the phase changes are similar to those found in nature.

The lead lag relationships are not as robust between some components as observational data show. They were also not always consistent with those patterns seen in previous studies using other models. However, this study did show that most of the components do correlate significantly with other components at certain lag times. In this model, the easterly components of SLP, the tropical SST field and the north Pacific SST field had shorter lag times, while the connections between westerly and easterly components had longer lag times. This may indicate that the PDO pattern may develop slightly faster on the eastern side of the Pacific basin, and slower in the western and central north Pacific, due to the lag from the Kuroshio Extension heat transport. As previous studies have stated, there are many outstanding issues in the

GCM representation of the climate system that can cause delayed or underestimated responses to events such as ENSO. In particular, solar radiation, cloud parameterizations and boundary layer interactions may have led to differences in the PDO phase change (Alexander 2002).

The smaller peaks in each of the lead-lag correlations at later lags imitate a cyclical pattern. Further research would be needed to understand how these later time periods are forced and if the PDO phase change is causing changes to the other fields that would show that the PDO has oscillatory features.

In summary, the proposed cycle of the PDO is supported by this modeled output. While some features are more robust than others, each of the components is supported by spatial EOF patterns and time series. The spectral density analysis indicates that each field has a signal at roughly the 12 to 18 year frequency, while the lead-lag relationships have high correlations at lags that indicate a cyclical pattern. While much is still to be understood of the mechanisms behind the complete cycle of the PDO, using modeled output that represents each of the components was a successful method for studying a long term oscillation for which observational data is limited.

REFERENCES

- Alexander, M. A., I. Bladé, M. Newman, J. R. Lanzante, N. C. Lau, J. D. Scott, 2002: The Atmospheric Bridge: The Influence of ENSO Teleconnections on Air–Sea Interaction over the Global Oceans. *J. Climate*, 15, 2205–2231.
- Biondi, F., A. Gershunov, D. R. Cayan, 2001: North Pacific Decadal Climate Variability since 1661. *J. Climate*, 14, 5–10.
- Buja, L. & T. Craig, 2002. CCSM2.0 User’s Guide. (Unpublished manuscript)
- Craig, Tony: CPL7 User’s Guide. NCAR (unpublished manuscript).
- Danabasoglu, G., W. G. Large, J. J. Tribbia, P. R. Gent, B. P. Briegleb, and J. C. McWilliams, 2006: Diurnal coupling in the tropical oceans of CCSM3. *J. Climate*, 19, 2347–2365.
- Danabasoglu, G., S. C. Bates, B. P. Briegleb, S. R. Jayne, M. Jochum, W. G. Large, S. Peacock and S. G. Yeager, 2012: The CCSM4 Ocean Component. *J. Climate*, 25, 1361-1389.
- Deser, C., A. Phillips, R. Tomas, Y. Okumura et al, 2011: ENSO and Pacific Decadal Variability in the Community Climate System Model Version 4. *J. Climate*, 25, 2622-2651.
- DiLorenzo, E., K.M. Cobb, J.C. Furtado, N. Schneider et al, 2010: Central Pacific El Nino and decadal climate change in the North Pacific Ocean. *Nature Geoscience*, 2, 762-765.
- Furtado, J. C., Di Lorenzo, E., Schneider, N., and Bond, N. A., 2011: North Pacific Decadal Variability and Climate Change in the IPCC AR4 Models. *J. Climate*, 24.
- Gent, P. R., G. Danabasoglu, L. J. Donner, M. M. Holland, E. C. Hunke, S. R. Jayne et al., 2011: The Community System Model Version 4. *J. Climate*, 24, 4973-4991.
- Hunke, E. C., W. H. Lipscomb, A. K. Turner, N. Jeffery, S. Elliott, 2013: CICE: The Los Alamos Sea Ice Model Documentation and Software User’s Manual Version 5.0. Los Alamos Nation Laboratory (unpublished manuscript).

- Kwon, Y. O. & C. Deser, 2006. North Pacific Decadal Variability in the Community Climate System Model Version 2. *J. Clim.*, 20.
- Kwon, M.H., S. W. Yeh, Y.G. Park & Y.K. Lee, 2012: Changes in the linear relationship of ENSO-PDO under the global warming. *Intl. Journal of Climatology*, 33, 1121-1128.
- Landrum, Laura, Bette L. Otto-Bliesner, Eugene R. Wahl, Andrew Conley, Peter J. Lawrence, Nan Rosenbloom, Haiyan Teng, 2013: Last Millennium Climate and Its Variability in CCSM4. *J. Climate*, 26, 1085–1111.
- Lian, T. & D. Chen, 2012. An Evaluation of Rotated EOF Analysis and Its Application to Tropical Pacific SST Variability. *J. Clim.*, 25, 5361-5373.
- Lienert, F. & F. J. Doblas-Reyes, 2013. Decadal prediction of interannual tropical and North Pacific sea surface temperature. *J. of Geo. Research*, 118.
- Lin, S. J., 2004: A “vertically Lagrangian” finite-volume dynamical core for global models. *Mon. Wea. Rev.*, 132, 2293–2307
- Los Alamos National Laboratory, 2010. Parallel Ocean Program (POP) User Guide Version 2.1.
- Mantua, N..J., S. Hare, Y. Zhang, J.M. Wallace, & R.C. Francis, 1997: A Pacific interdecadal climate oscillation with impacts on salmon production. *Bulletin of Am. Meter. Society*, 78.
- McCaa J. R., M. Rothstein, B. E. Eaton, J. M. Rosinski, E. Kluzek, M. Vertenstein, 2004: User’s Guide to the NCAR Community Atmosphere Model (CAM 3.0). NCAR (Unpublished manuscript).
- Neale, R. B., J. H. Richter, A. J. Conley, S. Park, P. H. Lauritzen, A. Gettelman, D. L. Williamson et al, 2010: Description of the NCAR Community Atmosphere Model (CAM 4.0). NCAR (unpublished manuscript).
- Park, J.H., S. I. An, S.W. Yeh, N. Schneider, 2013: Quantitative assessment of the climate components driving the pacific decadal oscillation in climate models. *Theoretical and Applied Climatology*, 112, 431-445.
- Pacific Decadal Oscillation Graphics. Joint Institute for the Study of the Atmosphere and Ocean. University of Washington, Seattle, WA.
http://jisao.washington.edu/pdo/img/pdo_warm_cool.ps
- Pierce, D. W., T. P. Barnett, N. Schneider, R. Saravanan, D. Dommengeset & M. Latif,

2001. The role of ocean dynamics in producing decadal climate variability in the North Pacific. *Climate Dynamics*, 18, 51-70.
- Qiu, Bo, 2003: Kuroshio Extension Variability and Forcing of the Pacific Decadal Oscillations: Responses and Potential Feedback. *J. Phys. Oceanogr.*, 33, 2465–2482.
- Oleson, K. W., D. M. Lawrence, G. B. Bonan, M. G. Flanner, E. Kluzek, P. J. Lawrence, S. Levis, S. C. Swenson and P. E. Thornton, 2010: Technical Description of version 4.0 of the Community Land Model (CLM). NCAR (Unpublished manuscript).
- Oshima, K. & Y. Tanimoto, 2009: An Evaluation of Reproducibility of the Pacific Decadal Oscillation in the CMIP3 Simulations. *J. of Met. Society of Japan*, 87, 755-770.
- Roe, G 2009. Feedbacks, Timescales and Seeing Red. *Ann. Review of Earth and Planetary Sciences*, 37.
- Schneider, N. & B. D. Cornuelle, 2005: The Forcing of the Pacific Decadal Oscillation. *J. Climate*, 18, 4355–4373.
- Smith, R., P. Jones, B. Briegleb, F. Bryan, G. Danabasoglu, J. Dennis et al, 2010: The Parallel Ocean Program (POP) Reference Manual. NCAR (unpublished manuscript).
- Stoner, A.M. K., K. Hayhoe, D. J. Wuebbles, 2009: Assessing General Circulation Model Simulations of Atmospheric Teleconnection Patterns. *J. Climate*, 22, 4348–4372.
- Taguchi, B., S-P Xie, N. Schneider, M. Nonaka, H. Sasaki, Y. Sasai, 2007: Decadal Variability of the Kuroshio Extension: Observations and an Eddy-Resolving Model Hindcast. *J. Climate*, 20, 2357–2377.
- Vertenstein, M., T. Craig, A. Middleton, D. Feddema, C. Fischer. CCSM4.0 User's Guide. (Unpublished manuscript).
- Wang, H., A. Kumar, W. Wang, Y. Xue, 2012: Influence of ENSO on Pacific Decadal Variability: An Analysis Based on the NCEP Climate Forecast System. *J. Climate*, 25, 6136–6151.
- Wang, B., R. Wu, X. Fu, 2000: Pacific–East Asian Teleconnection: How Does ENSO Affect East Asian Climate?. *J. Climate*, 13, 1517–1536.

- Yeo, S.R., K.Y. Kim, S.W. Yeh & W. Kim, 2012: Decadal changes in the relationship between the tropical Pacific and the North Pacific. *J. of Geophys. Research*, 117.
- Yu, J.Y., & Kim S. T., 2011: Relationships between Extratropical Sea Level Pressure Variations and the Central Pacific and Eastern Pacific Types of ENSO. *J. Clim.*, 24.
- Zhong, Y., Z. Liu, R. Jacob, 2008: Origin of Pacific Multidecadal Variability in Community Climate System Model, Version 3 (CCSM3): A Combined Statistical and Dynamical Assessment. *J. Climate*, 21, 114–133.

Appendix A

EQUATIONS FOR MODEL COMPONENTS

Governing Equations for Hydrostatic Atmosphere

Hydrostatic Balance

$$\frac{1}{\rho} \frac{\partial p}{\partial z} + g = 0$$

Conservation of Mass

$$\frac{\partial}{\partial t} \pi + \nabla \cdot (V\pi) = 0$$

First Law of Thermodynamics

$$\frac{\partial}{\partial t} (\pi\Theta) + \nabla \cdot (V\pi\Theta) = 0$$

Momentum Equations

$$\begin{aligned} \frac{\partial}{\partial t} u &= \Omega v - \frac{1}{A \cos \theta} \left[\frac{\partial}{\partial \lambda} (\kappa + \Phi - vD) + \frac{1}{\rho} \frac{\partial}{\partial \lambda} p \right] - \frac{d\zeta}{dt} \frac{\partial u}{\partial \zeta} \\ \frac{\partial}{\partial t} v &= \Omega u - \frac{1}{A} \left[\frac{\partial}{\partial \theta} (\kappa + \Phi - vD) + \frac{1}{\rho} \frac{\partial}{\partial \theta} p \right] - \frac{d\zeta}{dt} \frac{\partial v}{\partial \zeta} \end{aligned}$$

Governing Equations for Ocean Model

Momentum Equations

$$\begin{aligned} \frac{\partial}{\partial t} u + \mathcal{L}(u) - \frac{(uv \tan \phi)}{a} - fv &= -\frac{1}{\rho_0 a \cos \phi} \frac{\partial p}{\partial \lambda} + \mathcal{F}_{Hx}(u, v) + \mathcal{F}_V(u) \\ \frac{\partial}{\partial t} v + \mathcal{L}(v) - \frac{(u^2 \tan \phi)}{a} - fu &= -\frac{1}{\rho_0 a} \frac{\partial p}{\partial \phi} + \mathcal{F}_{Hy}(u, v) + \mathcal{F}_V(v) \\ \mathcal{L}(\alpha) &= \frac{1}{a \cos \phi} \left[\frac{\partial}{\partial \lambda} (u\alpha) + \frac{\partial}{\partial \phi} (\cos \phi v\alpha) \right] + \frac{\partial}{\partial z} (w\alpha) \\ \mathcal{F}_{Hx}(u, v) &= A_M \left\{ \nabla^2 u + \frac{u(1 - \tan^2 \phi)}{a^2} - \frac{2 \sin \phi}{a^2 \cos^2 \phi} \frac{\partial}{\partial \lambda} \right\} \end{aligned}$$

$$\mathcal{F}_{Hy}(u, v) = A_M \left\{ \nabla^2 v + \frac{v(1 - \tan^2 \phi)}{a^2} - \frac{2 \sin \phi}{a^2 \cos^2 \phi} \frac{\partial}{\partial \lambda} \right\}$$

$$\nabla^2 \alpha = \frac{1}{a^2 \cos^2 \phi} \frac{\partial^2 \alpha}{\partial \lambda^2} + \frac{1}{a^2 \cos \phi} \frac{\partial}{\partial \phi} \left(\cos \phi \frac{\partial \alpha}{\partial \phi} \right)$$

$$\mathcal{F}_V(\alpha) = \frac{\partial}{\partial z} \mu \frac{\partial}{\partial z} \alpha$$

Continuity Equation

$$\mathcal{L}(1) = 0$$

Hydrostatic Equation

$$\frac{\partial p}{\partial z} = -\rho g$$

Equation of State

$$\rho = \rho(\Theta, S, p) \rightarrow \rho(\Theta, S, z)$$

Tracer transport

$$\frac{\partial}{\partial t} \varphi + \mathcal{L}(\varphi) = \mathcal{D}_H(\varphi) + \mathcal{D}_V(\varphi)$$

$$\mathcal{D}_H(\varphi) = A_H \nabla^2 \varphi$$

$$\mathcal{D}_V(\varphi) = \frac{\partial}{\partial z} \kappa \frac{\partial}{\partial z} \varphi$$